ISSN: 1999-6691, e-ISSN: 2782-3709 DOI: http://doi.org/10.7242/1999-6691/2025.18.2.10

Research article

MHD-stirring of heavy impurities in a rotating magnetic field generated by a multi-section inductor

***R.S. Okatev*[1], *G.L. Losev*[1], *I.V. Kolesnichenko*[1]**

Institute of Continuous Media Mechanics UB RAS, Perm, Russian Federation

The efficiency of stirring a two-phase dispersed fluid like liquid metal with impurity particles in a cylindrical cell is investigated numerically using a multiphase two-fluid model. Stirring is driven by the electromagnetic force generated by a sectional rotating magnetic field inductor consisting of six annular segments evenly distributed along the height of the cell. Each segment generates a rotating magnetic field independently. We consider three electromagnetic force configurations. The first configuration corresponds to a co-directional rotation of the magnetic fields of all six inductors, matching the case of a classical rotating magnetic field. In the second configuration, three upper rings generate magnetic fields rotating in the same direction, and the lower three rings produce magnetic fields that also rotate in the same but opposite direction to the upper rings. In the third configuration, the directions of magnetic field rotation are altered along the cell height. We introduce a parameter for impurity distribution inhomogeneity. It is shown that the best stirring effect is achieved in the second configuration, which is attributed to the emergence of a large-scale oscillatory flow regime. The uniform rotating magnetic field configuration provides the least efficient stirring because it generates a low poloidal velocity. In the third configuration, the impurity distribution inhomogeneity parameter shows oscillations that are linked to the chaotic nature of the flow. The stirring time, where the impurity distribution inhomogeneity is minimal, is determined.

Keywords: sectional inductor, rotating magnetic field, magnetohydrodynamics, impurity stirring, multiphase media, numerical simulation

Received: 28.04.2025 / *Published online*: 30.07.2025

1. Introduction

Liquid metal stirring is a significant technological challenge in fields of metallurgy, foundry production, semiconductor industry, and materials science. Effective control over the flows involved in the stirring process makes it possible to homogenize the melt composition, improve the quality of castings, intensify crystallization processes, and eliminate alloy segregation.

High temperatures and the chemical aggressiveness of liquid metals require contactless methods. Due to a material's ability to conduct electric current, it becomes possible to generate flow within it by means of an alternating magnetic field [1]. When an alternating magnetic field is applied to an electrically conductive fluid, a volumetric Lorentz force is generated, which drives the motion. Electromagnetic stirring, unlike mechanical stirring, does not require contact with the melt, which reduces the risk of contamination with undesirable chemical elements and prevents premature wear of the equipment.

A rotating magnetic field (RMF) is a common tool to apply electromagnetic influence to liquid metals. Under the RMF, the homogeneity of a melt increases, alloying elements are redistributed, and nonmetallic inclusions (oxides, salts, slags) are removed by resulting centrifugal and electromagnetic forces [2]. The RMF makes it possible to control the rate of crystallization and the intensity of heat and mass transfer by eliminating temperature inhomogeneities at a crystallyzation front. In addition, it can suppress dendrite formation and promote the development of a fine-grained structure [3–5]. The RMF can also improve the properties of composite materials by ensuring a more uniform distribution of reinforcing particles in the metal (for example, in steel and aluminum composites) [6, 7]. In the production of single crystals of silicon and other semiconductors, the RMF is used to control heat and mass transfer in the melt, thereby reducing crystal defects [8, 9].

One of the main problems with the application of classical RMF is the low intensity of secondary poloidal flows [10]. The consequence of this is poor stirring efficiency and, as a result, non-uniform distribution of temperature or impurities in a melt. The quality of the final product can be improved by increasing the complexity of the flow topology, for instance, by changing the position of an inductor relative to the liquid-metal cell during stirring, or by varying the amplitude and frequency of the magnetic field [11, 12]. Stirring efficiency can be enhanced by modulating the power supply of an RMF inductor [13, 14], and by changing the field direction or by alternating on/off power supply [15–17]. Another way to enhance poloidal flow intensity is to combine the RMF with a traveling magnetic field [18]. However, although the combined action improves stirring efficiency compared to the classical RMF, it still results only in large-scale flow structures characterized by spatial nonuniformity of the velocity field and the presence of stagnant zones in the conductive fluid volume. Therefore, the degree of homogeneity of the resulting ingots decreases. Thus, there arises

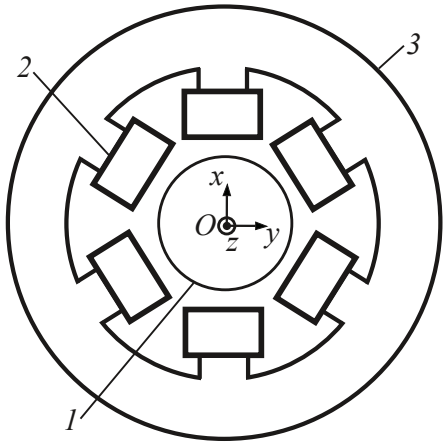

Figure 1. Top view of the annular inductor: *1* – cylinder filled with liquid metal; *2* – generating coils; *3* – magnetic core

the problem of finding other ways to complicate the topology of the imposed magnetic field and thereby to improve the efficiency of stirring of the electrically conductive medium.

It is also possible to make the poloidal flow more intense without combining it with a traveling field. For this purpose, RMF inductors should be designed in such a way that they will be able to generate counter-directed flows, i.e., to produce local instability regions characterized by a high degree of velocity fluctuations [19]; this should theoretically enhance stirring efficiency. In this work, the efficiency of heavy-impurity stirring in a cylindrical cell filled with liquid metal and placed in a sectional electromagnetic stirrer based on the RMF is numerically investigated for three different configurations of the generated magnetic field and the electromagnetic force.

2. Problem statement

We consider a flow that arises in a cylindrical cell with conducting fluid *1*; the axis of rotation of the cell coincides with the direction of gravity. The flow is generated in the cell by the electromagnetic forces created by an inductor. The inductor consists of six identical rings, each including six coil segments *2* connected by vertical magnetic cores that generate a magnetic field. The coils are placed on the protruding parts of the magnetic core *3* (Fig. 1). The inductor of this design is capable of producing an electromagnetic field and, consequently, a volumetric force of different spatial topologies, which makes it possible to mix the flows of different scales and intensities. The inductor's geometry is based on the physical prototype previously used for verification of electromagnetic and hydrodynamic simulations (see [20, 21]).

The basic element of the inductor is a single ring composed of six coil segments that generate a magnetic field. By stacking six basic elements vertically and assigning different RMF directions to each, it is possible to create various configurations of electromagnetic force and, consequently, different flow structures. Three configurations are considered in this work:

1) homogeneous rotating magnetic field (HRMF) — all inductor rings generate magnetic fields rotating in the same direction;

2) two-section rotating magnetic field (TRMF) — three upper rings of the inductor generate magnetic fields rotating clockwise, while three lower rings produce fields rotating counterclockwise;

3) multi-section rotating magnetic field (MRMF) — each inductor ring generates a magnetic field rotating in the direction opposite to that of its neighboring rings, i.e., the directions of the electromagnetic forces alternate along the cylinder height.

A schematic representation of these configurations is shown in Fig. 2. The figure also indicates the orientation of the Cartesian coordinate system axes. For convenience, the results are recorded a cylindrical coordinate system, the origin of which coincides with that of the Cartesian system, and the relations between the radial and azimuthal components of vectors and their corresponding Cartesian components are given by the standard formulas.

3. Mathematical model

The mathematical model describing the process of stirring a liquid metal with heavy impurity particles under the action of RMF within the computational domain is based on the magnetohydrodynamic equations for a viscous incompressible fluid (Fig. 1). The parameter characterizing the interaction between the conductive fluid flow and the magnetic field is the magnetic Reynolds number $\mathrm{Re_m} = \sigma\mu\mu_0 UL$, where σ is the electrical conductivity of the medium,

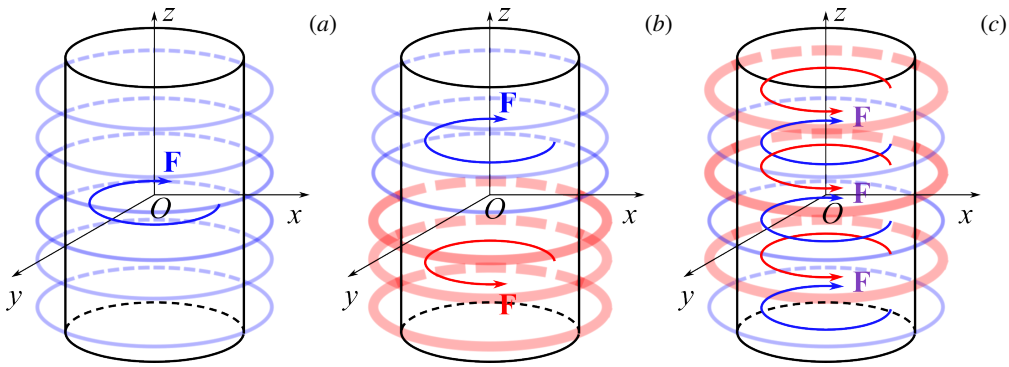

Figure 2. Three considered configurations of the magnetic field and electromagnetic force: HRMF (*a*), TRMF (*b*), MRMF (*c*); clockwise rotation of the magnetic field is shown by a thin line, and counterclockwise rotation by a thick line; the vector of the resulting twisting electromagnetic force **F** is shown by an open-ended arrowhead line

μ is the magnetic permeability, $\mu_0 = 4\pi \cdot 10^{-7}$ H/m is the magnetic constant, and U and L are the characteristic velocity and length scale of the conducting medium within the study region. According to the preliminary estimates provided by the authors of this work, in the formulated problem, $\mathrm{Re_m} \ll 1$. Therefore, the influence of the flow on the magnetic field can be neglected. Moreover, the solution of the problem is done in the electrodynamic approximation, since the currents induced by the fluid motion are small compared to the imposed ones. Therefore, the coupled MHD problem can be separated into two subproblems: electrodynamic and hydrodynamic.

The key assumption for the electrodynamic subproblem is that a liquid metal is treated as a homogeneous medium without impurity particles, i.e., a medium with uniform conductivity similar to that of the fluid $\sigma = 2.6$ MS/m. Based on the models of effective conductivity [22], estimates for the typical impurity volume fraction $\varphi \approx 1\%$ and particle conductivity $\sigma_\mathrm{s} = 50$ MS/m show that the deviations in the overall electrical conductivity and the resulting electromagnetic force do not exceed 10%. However, taking these effects into account could significantly increase computational costs due to the need for solving a coupled problem with recalculation of the electrodynamic component at each time step. Therefore, they are neglected in the present study. It should also be noted that the electromagnetic force acting on the dispersed phase in the fluid arises from a difference in electrical (phase) conductivity, and it is considered while solving the hydrodynamic subproblem.

The mathematical formulation of the electrodynamic subproblem includes Maxwell's electrodynamic equations:

$$\begin{aligned} \nabla \times \mathbf{H} &= \mathbf{j}_\mathrm{c}, \\ \nabla \times \mathbf{E} &= -\frac{\partial \mathbf{B}}{\partial t}, \\ \nabla \cdot \mathbf{B} &= 0, \\ \nabla \cdot \mathbf{E} &= 0, \end{aligned} \tag{1}$$

where $\mathbf{H}$ is the magnetic field intensity, $\mathbf{j}_\mathrm{c}$ is the alternating current density in the generating coils, $\mathbf{E}$ is the electric field intensity, and $\mathbf{B} = \mu\mu_0\mathbf{H}$ is the magnetic flux density. The alternating current of frequency f passing through the coils generates a time-varying magnetic field. This field, in turn, induces a variable eddy electric field $\mathbf{E}$, which produces eddy currents in conductive volumes.The density of these currents is determined by Ohm's law:

$$\mathbf{j} = \sigma \mathbf{E}.$$

When solving the electrodynamic subproblem, we determine the distribution of the electromagnetic force in the liquid-metal cell and in the surrounding space, caused by the interaction between the induced eddy currents and the magnetic field:

$$\mathbf{F}^\mathrm{em} = \mathbf{j} \times \mathbf{B}. \tag{2}$$

The electrodynamic subproblem (1), (2) is solved in harmonic formulation using the finite element software package ANSYS Emag. The implementation algorithm was described earlier in [19, 21, 23]. It is based on the unstructured tetrahedral mesh with approximately $2 \cdot 10^6$ elements. Different RMF configurations are modeled by specifying appropriate phase distributions of the coil currents. For all RMF configurations, the current frequency ($f = 50$ Hz) and the current amplitude (1 A) in the coils are fixed. Each coil contains 998 turns. For all computational domain elements,

except magnetic cores, the magnetic permeability μ is set to unity. The magnetic permeability of the ferromagnetic cores is assumed constant and equal to $3.3\cdot10^3$. Eddy currents are considered to be generated only in a liquid-metal cell.

Next, by solving the hydrodynamic subproblem, we determine the flow characteristics of the two-phase conducting fluid in a cylindrical cell of radius 48 mm and height 300 mm. The fluid motion is driven by the electromagnetic force (2), whose field is already known from the electrodynamic solution. The two-phase fluid is described using the multi-velocity approach [24], according to which both phases are treated as interpenetrating fluids, each occupying the entire computational domain and characterized by its volume fraction. Let the impurity phase volume fraction be denoted by φ, and that of the fluid by $1-\varphi$. For convenience, in all relations, the quantities related to the dispersed phase (except φ) are marked with a subscript s, while those related to the primary phase (fluid) have no subscript. Then, the continuity and momentum equations for both phases can be written as:

$$\begin{gathered}
\frac{\partial}{\partial t}((1-\varphi)\rho)+\nabla\cdot((1-\varphi)\rho\mathbf{u})=0,\\
\frac{\partial}{\partial t}(\varphi\rho_{\mathrm{s}})+\nabla\cdot(\varphi\rho_{\mathrm{s}}\mathbf{u}_{\mathrm{s}})=0,\\
\frac{\partial}{\partial t}((1-\varphi)\rho\mathbf{u})+\nabla\cdot((1-\varphi)\rho\mathbf{u}\mathbf{u})=-(1-\varphi)\nabla p+\nabla\cdot\mathbf{T}+(1-\varphi)\rho\mathbf{g}+K(\mathbf{u}_{\mathrm{s}}-\mathbf{u})+\mathbf{F}^{\mathrm{em}},\\
\frac{\partial}{\partial t}(\varphi\rho\mathbf{u}_{\mathrm{s}})+\nabla\cdot(\varphi\rho\mathbf{u}_{\mathrm{s}}\mathbf{u}_{\mathrm{s}})=-\varphi\nabla p-\nabla p_{\mathrm{s}}+\nabla\cdot\mathbf{T}_{\mathrm{s}}+\varphi\rho_{\mathrm{s}}\mathbf{g}-K(\mathbf{u}_{\mathrm{s}}-\mathbf{u})+\mathbf{F}_{\mathrm{s}}^{\mathrm{lift}}+\mathbf{F}_{\mathrm{s}}^{\mathrm{em}}.
\end{gathered}\tag{3}$$

In equations (3), ρ is the density of the fluid, ρ_{s} is the density of the dispersed phase, $\mathbf{u}$ and $\mathbf{u}_{\mathrm{s}}$ are the velocity vectors of the primary and dispersed phases, K is the interphase interaction coefficient, $\mathbf{T}$ and $\mathbf{T}_{\mathrm{s}}$ are the viscous stress tensors of the primary and dispersed phases, $\mathbf{F}_{\mathrm{s}}^{\mathrm{lift}}$ and $\mathbf{F}_{\mathrm{s}}^{\mathrm{em}}$ are the lifting and electromagnetic forces acting on the dispersed phase, and p_{s} is the granular pressure.

The primary phase is treated as a viscous incompressible fluid, therefore the expression for the viscous stress tensor is given as:

$$\mathbf{T}=(1-\varphi)\eta\left(\nabla\mathbf{u}+\nabla\mathbf{u}^{\mathrm{T}}\right),$$

where $\eta=\eta_{\mathrm{m}}+\eta_{\mathrm{t}}$ is the effective viscosity consisting of the dynamic and turbulent components.

The dispersed phase is described within the framework of the granular flow model [25, 26]. The viscous stress tensor in this case has the same form as that for a compressible viscous fluid:

$$\mathbf{T}_{\mathrm{s}}=\varphi(\zeta_{\mathrm{s}}-(2/3)\eta_{\mathrm{s}})(\nabla\cdot\mathbf{u}_{\mathrm{s}})\mathbf{I}+\varphi\eta_{\mathrm{s}}\left(\nabla\mathbf{u}_{\mathrm{s}}+\nabla\mathbf{u}_{\mathrm{s}}^{\mathrm{T}}\right).$$

The specific feature of the granular model is that the bulk (ζ_{s}) and dynamic (η_{s}) viscosities of the dispersed phase, as well as the granular pressure, are determined by applying the kinetic equations constructed analogously to those for gaseous media. The quantity

$$p_{\mathrm{s}}=\varphi\rho_{\mathrm{s}}\Theta_{\mathrm{s}}+2\rho_{\mathrm{s}}(1+e_{\mathrm{ss}})\varphi^2 g_0\Theta_{\mathrm{s}},$$

called the granular pressure, describes the pressure variation in the dispersed phase due to kinetic effects and particle–particle collisions [27, 28]. Here, Θ_{s} is the granular temperature, which, similarly to thermodynamic temperature, represents a measure of the mean kinetic energy of the random motion of impurity particles [29], g_0 is the empirical radial distribution function,

$$g_0=\left[1-(\varphi/\varphi_{\max})^{1/3}\right]^{-1},$$

and e_{ss} is the coefficient of restitution, which equals 0.9 for perfectly elastic particle collisions.

In calculating the dynamic viscosity, as in the expression for granular pressure, we take into account the contributions associated with the transfer of momentum by the random motion of impurity particles (kinetic component) and by their collisions (collisional component) [30]:

$$\eta_{\mathrm{s}}=\eta_{\mathrm{s}}^{\mathrm{kin}}+\eta_{\mathrm{s}}^{\mathrm{col}}.$$

The main contribution comes from the kinetic viscosity, which is given by:

$$\eta_{\mathrm{s}}^{\mathrm{kin}}=\frac{d_{\mathrm{s}}\rho_{\mathrm{s}}\sqrt{\Theta_{\mathrm{s}}\pi}}{6(3-e_{\mathrm{ss}})}[1+(2/5)(1+e_{\mathrm{ss}})(3e_{\mathrm{ss}}-1)g_0\varphi],$$

where d_{s} is the particle diameter. At large impurity volume fractions, the collisional viscosity contribution

$$\eta_{\mathrm{s}}^{\mathrm{col}}=(4/5)\varphi\rho_{\mathrm{s}}d_{\mathrm{s}}g_0(1+e_{\mathrm{ss}})\sqrt{\Theta_s/\pi}$$

becomes dominant.

Compressibility effects associated with bulk viscosity turn out to be small because its coefficient depends quadratically on the impurity volume fraction φ [31]:

$$\zeta_{\rm s} = (4/3)\varphi^2 \rho_{\rm s} d_{\rm s} g_0 (1+e_{\rm ss}) \sqrt{\Theta_s/\pi}.$$

In the model used, the total force acting on the dispersed phase is composed of lifting and electromagnetic components. The lifting force

$$\mathbf{F}_{\rm s}^{\rm lift} = -C_l \varphi \rho (\mathbf{u}-\mathbf{u}_{\rm s}) \times (\nabla \times \mathbf{u})$$

is associated with the local velocity gradients of the primary phase and reaches its maximum near the walls. The coefficient C_l is a nonlinear empirical function of the particle Reynolds number, which is determined by the particle diameter [32]:

$$\mathrm{Re}_{\rm p} = \frac{\rho |\mathbf{u}-\mathbf{u}_{\rm s}| d_{\rm s}}{\eta}.$$

The electromagnetic force acting on the dispersed phase depends on the difference in conductivities between the phases and can be estimated using the expression derived for a single spherical particle [33, 34]:

$$\mathbf{F}_{\rm s}^{\rm em} = \frac{3V_p}{2}\left(\frac{\sigma-\sigma_{\rm s}}{2\sigma+\sigma_{\rm s}}\right)\mathbf{F}^{\rm em} = \frac{3V_{\rm p}}{2}\left(\frac{\sigma-\sigma_{\rm s}}{2\sigma+\sigma_{\rm s}}\right)(\mathbf{j}\times\mathbf{B}),$$

where $V_{\rm p}$ is the particle volume, and $\mathbf{F}^{\rm em} = \mathbf{j}\times\mathbf{B}$ is the electromagnetic force acting on the fluid in the absence of a particle. Assuming that all particles are spherical and have the same diameter, we obtain the expression for the electromagnetic force density acting on the dispersed phase:

$$\mathbf{F}_{\rm s}^{\rm em} = \frac{3\varphi}{2}\left(\frac{\sigma-\sigma_{\rm s}}{2\sigma+\sigma_{\rm s}}\right)(\mathbf{j}\times\mathbf{B}).$$

The interaction between the phases is described by the coefficient K, for which we use the formula [35]:

$$K = \frac{3\varphi(1-\varphi)\rho}{4 v_{\rm r}^2 d_{\rm s}} C_D |\mathbf{u}_{\rm s}-\mathbf{u}|,$$

where C_D is the drag coefficient, and $v_{\rm r}$ is the mean relaxation velocity of a particle related to its free motion under the equilibrium of buoyancy, gravity, and drag forces. For the drag coefficient, we use a generalized Stokes model [36]:

$$C_D = \left(0.63 + \frac{4.8}{\sqrt{\mathrm{Re}_{\rm p}/v_{\rm r}}}\right)^2.$$

The expression for the particle relaxation velocity is given by [37]:

$$v_{\rm r} = \frac{1}{2}\left(A - 0.06\mathrm{Re}_{\rm p} + \sqrt{0.06\mathrm{Re}_{\rm p}{}^2 + 0.12\mathrm{Re}_{\rm p}(2B-A) + A^2}\right),$$

where the parameters A and B depend on the impurity volume fraction:

$$A = (1-\varphi)^{4.14}, \quad B = \begin{cases} (1-\varphi)^{2.65}, & \varphi \leqslant 0.15, \\ 0.8(1-\varphi)^{1.28}, & \varphi > 0.15. \end{cases}$$

The hydrodynamic subproblem (3) is solved by the finite volume method implemented in the ANSYS Fluent computational fluid dynamics package. For this purpose, the computational domain is discretized by a mesh with $2.7\cdot10^5$ tetrahedral elements near the side walls. A constant time step of 0.1 s is employed. Flow turbulence is modeled in terms of the SST k–ω model. Data transfer from the electrodynamic mesh to the hydrodynamic one is performed using a custom Python script. The fluid is assumed to have the properties of the eutectic Ga–Sn–Zn alloy [38]: $\rho = 6150$ kg/m^3, $\eta = 1.75\cdot10^{-3}$ Pa·s, and $\sigma = 2.6$ MS/m. The dispersed-phase particle density is 10% higher than that of the primary phase and equals $\rho_{\rm s} = 6765$ kg/m^3. As impurities, we consider spherical particles with a diameter of 50 μm and conductivity of $\sigma_{\rm s} = 50$ MS/m. Additionally, a constant value of 0.535 N/m is used to represent interfacial surface tension.

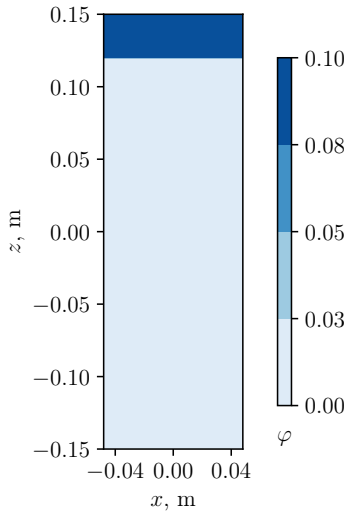

Figure 3. Initial impurity distribution (the cross-section of the cell by the Oxz plane of the Cartesian coordinate system)

4. Results

Let us analyze the flow structures generated in the conducting fluid for different configurations of external forces, as well as the process of impurity transport by these flows. As the initial state of the system, we consider a quiescent state where the fluid velocity is zero throughout the working volume. The initial impurity distribution is specified as a localized region in the upper part of the computational domain, 30 mm thick, with an impurity volume fraction $\varphi = 0.1$. Outside this region, the impurity volume fraction is set to zero. The initial impurity distribution is shown in Fig. 3.

The application of external electromagnetic forces at $t = 0$ causes the fluid to move and this, in turn, initiates stirring. An azimuthally directed force promotes a large-scale rotational motion, which, due to the continuity of the medium and the finite dimensions of the working volume, induces a secondary poloidal flow. It is this secondary flow that provides the transport of impurity particles along the height of the cell. The velocity fields of the primary and dispersed phases are similar, with the velocity magnitude difference not exceeding 2%. Therefore, in the subsequent analysis, only the distributions of the fluid's poloidal velocity $\mathbf{u}_\mathrm{p}$ and the impurity volume fraction are presented.

Figures 4, 5, and 7 illustrate the distribution of the poloidal velocity magnitude and impurity volume fraction for three configurations of electromagnetic force at different times. All fields are shown in the Oxz plane of the Cartesian coordinate system (see Fig. 2). In this cross-section, the azimuthal velocity component u_φ coincides with the Cartesian component u_y, and the magnitude of the poloidal velocity is defined as

$$|\mathbf{u}_\mathrm{p}| = \sqrt{u_x^2 + u_z^2}.$$

The HRMF induces a quasi-solid-body rotation in the conductive fluid (Fig. 4). The pressure gradient associated with the centrifugal force produces two toroidal vortices in the medium due to fluid motion toward the low-pressure zones near the upper and lower cylinder ends. These vortices form a quasi-stationary flow pattern and maintain their intensity and size over time. The steady nature and relatively small magnitude of the poloidal velocity (of the order of 1 cm/s) result in low impurity stirring efficiency.

Heavy impurities, initially concentrated in the upper part of the cell, settle at the bottom of the fluid due to gravity. The large-scale rotational flow redistributes particle concentration in a radial direction and the subsequent partial homogenization of the dispersed phase distribution due to the influence of inertia forces. However, the intensity of secondary poloidal flows is insufficient to provide effective transport along the height of the cell. As a result, the concentration inhomogeneity develops along the Oz axis, and the impurity gradually accumulates in the bottom region. Particles that reach the lower part of the cell are almost not involved in a vertical motion, which prevents the uniform impurity distribution even at later times.

In the TRMF configuration (see Fig. 5), during the initial stage ($t = 0 \div 30$ s), a pair of secondary toroidal vortices gradually forms near the plane with the vertical coordinate $z = 0$. The tangential discontinuity of azimuthal velocity associated with the abrupt change in magnetic field direction leads to the formation of Kelvin–Helmholtz instability.

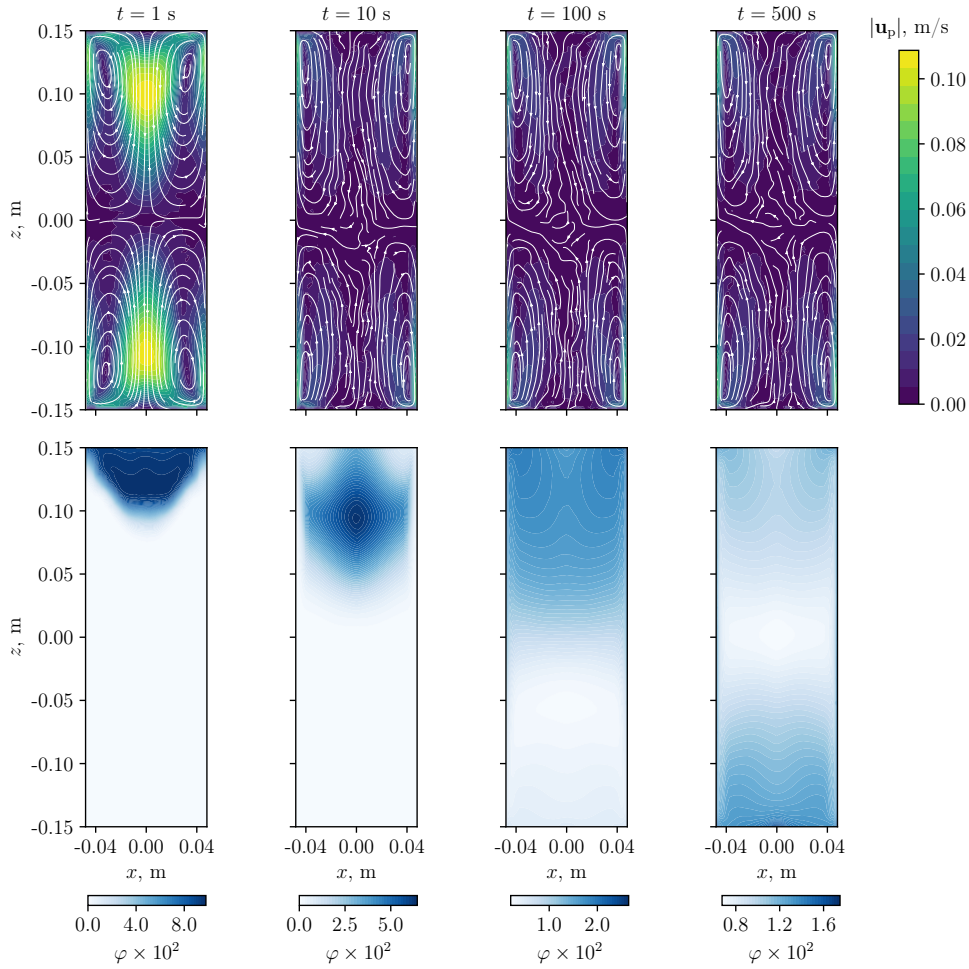

Figure 4. Fields of poloidal fluid velocity (top) and impurity volume fraction (bottom) for the HRMF configuration at different times

Because of the superposition of magnetic fields generated by the adjacent inductors producing oppositely directed magnetic fields, the local azimuthal inhomogeneity of the electromagnetic force arises, manifested itself as a reduction in the amplitude of a force action. This azimuthal nonuniformity, combined with the developing instability, leads to the formation of large-scale oscillatory regimes. Oscillations caused by periodic variations in vortex size break the symmetry of the poloidal velocity field with respect to the cylinder rotation axis. The evolution of the poloidal velocity component over one oscillation period (4 s) is shown in Fig. 6.

An oscillatory regime in the TRMF configuration drives intensive impurity stirring at the Kelvin–Helmholtz hydrodynamic instability. Moreover, two counter-rotating azimuthal vortices create a locking flow pattern that slows the settling of particles at the bottom of the cell. As a result, at moderate stirring time (up to $t = 500$ s), an almost uniform impurity distribution is achieved in the middle part of the cell, and a layer with reduced (at the top) and increased (at the bottom) impurity concentration is observed. Due to the moderate intensity of the poloidal flow and the presence of stagnant zones in the corners of the domain (see Fig. 5), the localized regions of the increased impurity volume fraction gradually appear over time.

In the MRMF configuration, a more complicated flow pattern occurs. The Kelvin–Helmholtz instability developing in all regions where the rotation direction of the magnetic field changes causes chaotic motion and leads to the formation of vortices of large and intermediate scales (see Fig. 7). In this case, the characteristic size of poloidal vortices is smaller than in the previously considered configurations. The irregular flow pattern persists over time, while the intensity fluctuates slightly around an average level. With the formation of a chaotic structure, the impurity transport through the cell volume slows down, and the settling velocity of heavy particles decreases. At the initial stirring stage (up to $t = 10$ s), due to the relatively low poloidal velocity, the diffusion of the initial concentration zone is weak. Later (at $t > 100$ s), the flow

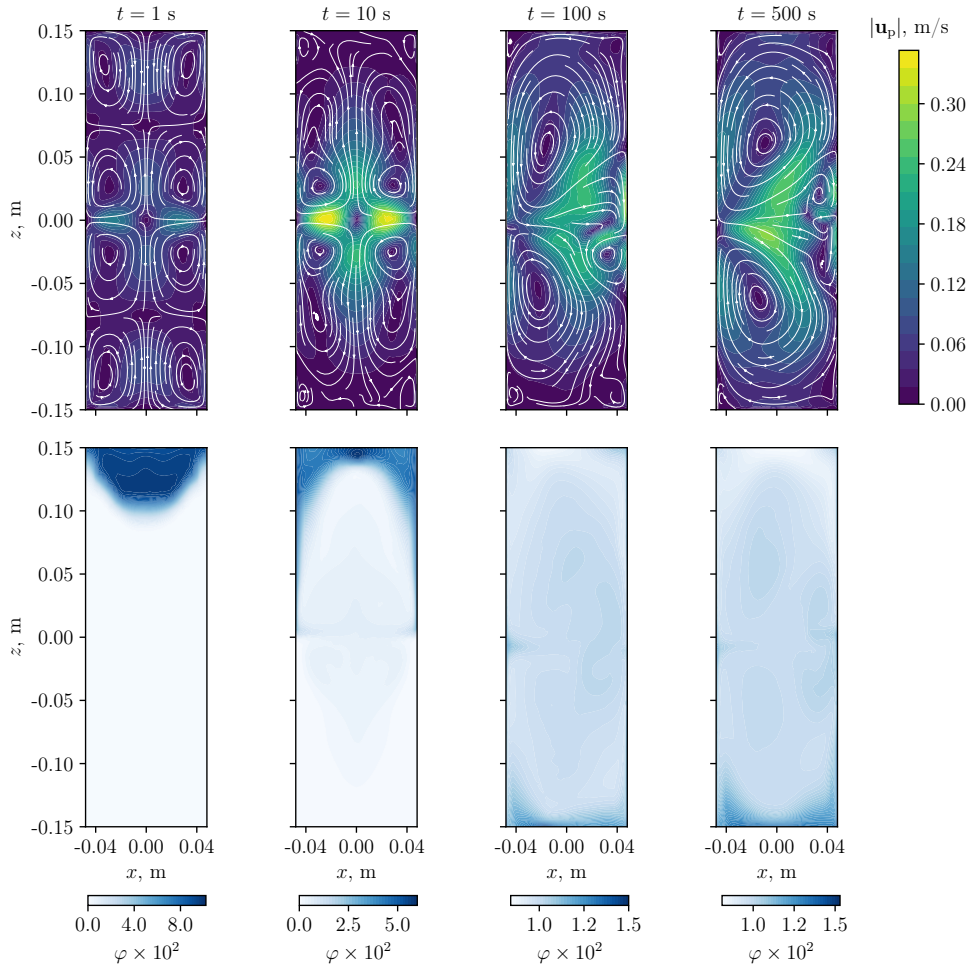

Figure 5. Fields of poloidal fluid velocity (top) and impurity volume fraction (bottom) for the TRMF configuration

structure becomes more complex, and this enhances stirring efficiency.

To quantitatively assess the degree of homogenization of the impurity distribution during stirring, we introduce the inhomogeneity parameter:

$$\tau(t) = \int_V (\varphi(t) - \varphi^*)^2 dV,$$

where $\varphi^* = 0.01$ is the impurity volume fraction corresponding to a homogeneous distribution over the volume. Figure 8 shows the time dependence of the inhomogeneity parameter, normalized by its initial value $\tau(0)$, for all configurations of the electromagnetic force (2). The HRMF shows the lowest level of stirring due to the small poloidal velocity component. Therefore, the impurity redistribution along the cell height occurs mainly due to gravitational settling. The region of weak variation of the inhomogeneity parameter in the graph at $t = 300 \div 500$ s is caused by the accumulation of part of the heavy impurity in the bottom layer, while the remaining fraction is entrained by the fluid flow. The minimum of the dependence corresponds to $t \approx 400$ s. At later times, τ increases due to the sedimentation of impurity particles and their accumulation in the bottom layer.

Stirring in the MRMF configuration is more effective. Nevertheless, the $\tau(t)$ curve for this regime exhibits irregular fluctuations of the parameter. These are caused by the transport of impurity from the bottom and near-wall regions toward the central part of the cell by the chaotic vortical motion. Thus, at identical parameters, the MRMF provides more effective long-term stirring compared to the homogeneous field.

The TRMF configuration exhibits the lowest inhomogeneity. It is worth to note that the time dependence of the inhomogeneity parameter $\tau(t)$ in this case has a well-defined minimum, which can be used to estimate the optimal stirring time. This minimum corresponds to the locking flow, which slows down particle settling and increases the time required

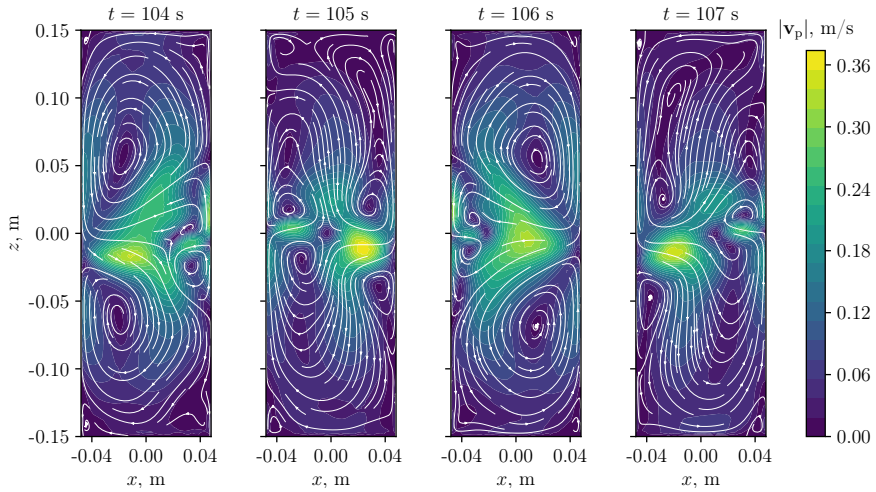

Figure 6. Fields of poloidal fluid velocity for the TRMF configuration during one period of large-scale oscillations

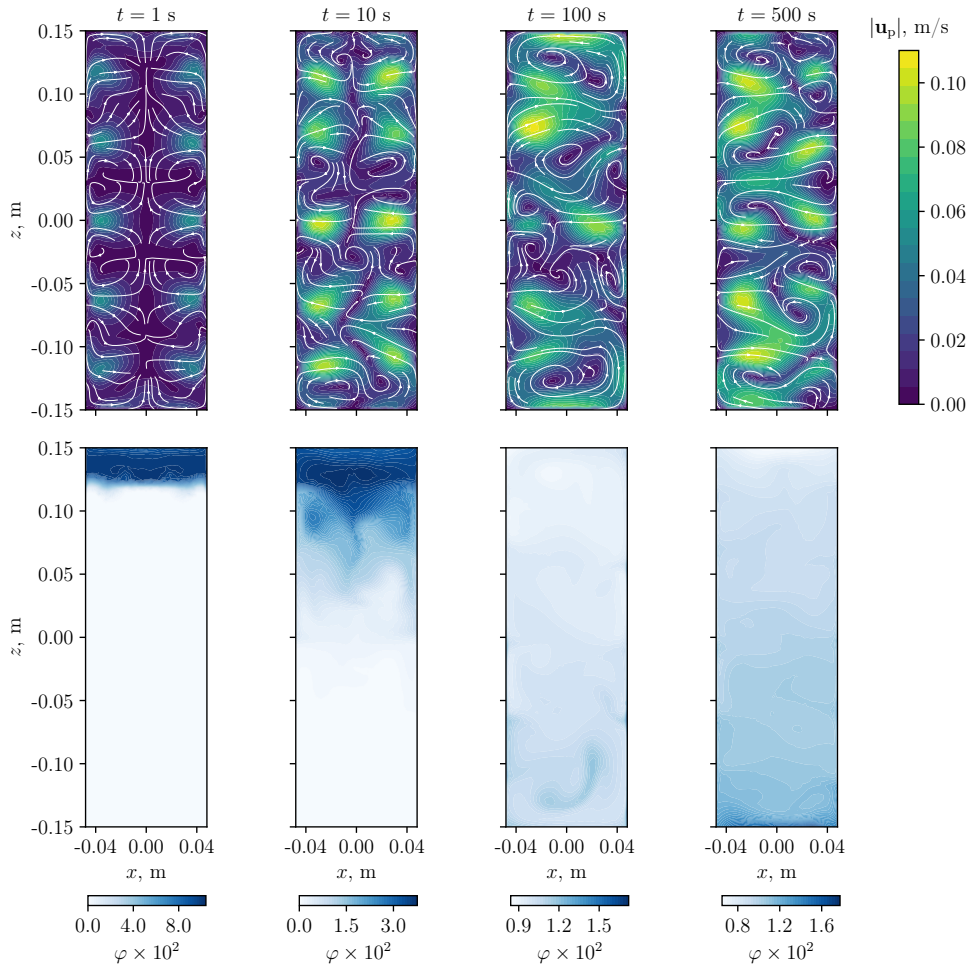

Figure 7. Fields of poloidal fluid velocity (top) and impurity volume fraction (bottom) in the MRMF configuration

for a uniform impurity distribution. After the minimum, the inhomogeneity parameter reaches a plateau region caused by the balance between sedimentation and re-entrainment of settled particles. Due to the sufficiently high intensity and

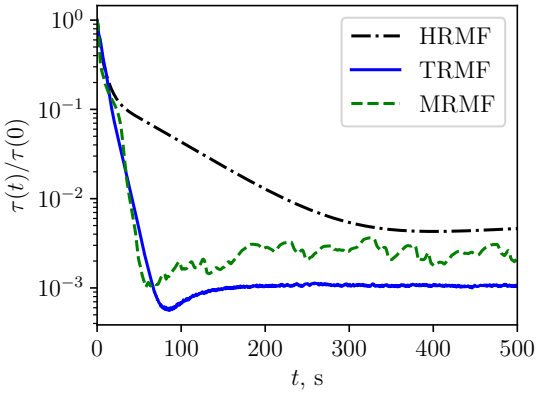

Figure 8. Time dependence of the normalized inhomogeneity parameter of the impurity distribution

unsteadiness of the flow for the chosen cell geometry and TRMF parameters, this configuration ensures most favorable stirring conditions.

5. Conclusion and discussion

The structure of flows in an electrically conducting two-phase medium was examined for different RMF configurations, and the evolution of the dispersed-phase volume fraction redistributed under the combined action of the induced flow and gravity was evaluated.

The HRMF generates a quasi-solid-body rotation of the fluid in the computational domain. The magnetic field of such a configuration corresponds to the classical stirring scheme but is characterized by a small poloidal velocity component, leading to low stirring efficiency.

The refinement of the vortex structure through unstable counter-rotating flows increases stirring efficiency. However, the magnetic field topology of the inductor limits the achievable flow intensity for the same power input as in other configurations. In addition, the high velocity pulsations lead to the occurence of unsteady stirring regimes and the trapping of impurities in vortices. It is necessary to note that the case under study does not concern small-scale turbulent velocity fluctuations (which affect effective diffusion), but rather the temporal variation of the mean (large-scale) velocity field.

As a measure of flow intensity, the kinetic energy of the flow components: poloidal

$$E_{\mathrm{p}} = \int\limits_V \left(u_r^2 + u_z^2\right) dV$$

and azimuthal

$$E_{\mathrm{t}} = \int\limits_V u_\phi^2 dV$$

was considered.

As seen in Fig. 9, the HRMF is characterized by a high value of E_{t} and a low value of E_{p}, differing by three orders of magnitude. The large-scale flow generation regime, in which a single pair of counter-rotating vortices is formed, proves to be the most effective for impurity stirring, as it produces a region of instability with strong velocity pulsations. In this case, the azimuthal flow energy decreases only slightly compared to the HRMF, while the poloidal flow energy increases by more than an order of magnitude. It was previously shown [19] that the MRMF regime is characterized by comparable values of E_{t} and E_{p}, and it is essential that this energy balance is obtained not only due to the increase of the poloidal component but also due to the weakening of the azimuthal flow compared to the HRMF configuration. This effect is associated with the azimuthal nonuniformity of the electromagnetic force arising at the junctions of oppositely rotating magnetic fields. In the TRMF regime, there is one such region of force reversal, which weakens the total force action and thus reduces the azimuthal flow energy. In the MRMF regime, the increased number of oppositely directed inductor pairs causes a more significant decrease in the effective force. The reduction in fluid rotation speed results in longer vortex restructuring times compared to the oscillation period observed in the TRMF regime.

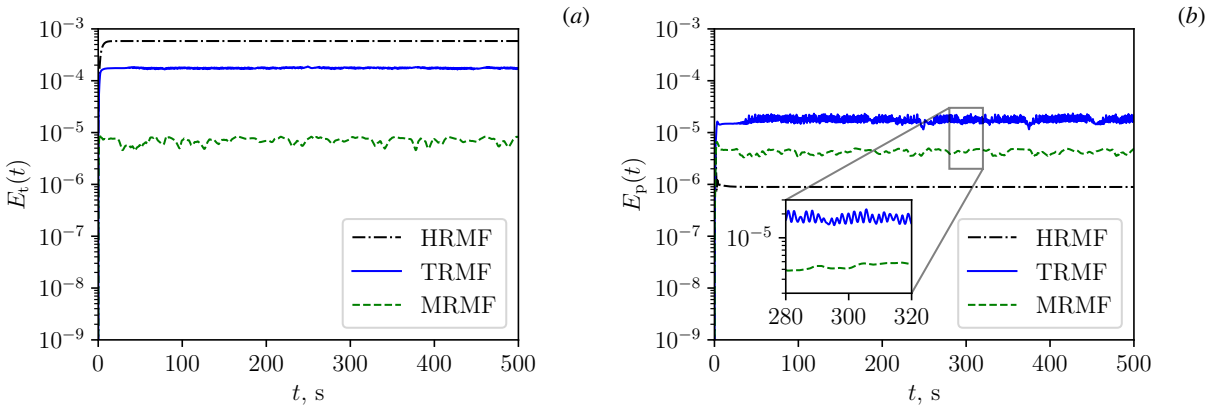

Figure 9. Time evolution of the kinetic energy of azimuthal (*a*) and poloidal (*b*) velocity components for the three rotating magnetic field configurations

The introduced inhomogeneity parameter shows that, for the cylindrical cell considered, the TRMF configuration, which produces pulsating poloidal vortices, provides the best homogenization. This result agrees with the conclusion of [39], which states that one of the key factors for improving impurity stirring quality is flow asymmetry. Moreover, there exists an optimal stirring time, determined by the physical properties of the fluid and the impurity, at which the degree of inhomogeneity reaches a minimum. Further stirring increases the concentration nonuniformity due to sedimentation of the dispersed phase and the formation of stagnant zones in the cell corners. The MRMF regime also exhibits a shallow minimum in the time dependence of impurity inhomogeneity; however, the chaotic flow nature prevents an unambiguous determination of the optimal stirring time because of multiple local extrema in $\tau(t)$. Nevertheless, the irregular spatiotemporal flow structure promotes the re-entrainment of settled impurity into the fluid flow, suggesting that, at longer times, the efficiency of stirring under MRMF conditions may exceed that achieved in the TRMF regime.

This work was carried out within the framework of the state assignment of the Institute of Continuous Media Mechanics, Ural Branch of the Russian Academy of Sciences (Project No. 124012300246-9).

References

1. *Moffatt H.K.* Electromagnetic stirring. Physics of Fluids A: Fluid Dynamics. 1991. Vol. 3, no. 5. P. 1336–1343. DOI: 10.1063/1.858062
2. *Jie J.C.*, *Zou Q.C.*, *Sun J.L.*, *Lu Y.P.*, *Wang T.M.*, *Li T.J.* Separation mechanism of the primary Si phase from the hypereutectic Al–Si alloy using a rotating magnetic field during solidification. Acta Materialia. 2014. Vol. 72. P. 57–66. DOI: 10.1016/j.actamat.2014.03.031
3. *Murty B.S.*, *Kori S.A.*, *Chakraborty M.* Grain refinement of aluminium and its alloys by heterogeneous nucleation and alloying. International Materials Reviews. 2002. Vol. 47, no. 1. P. 3–29. DOI: 10.1179/095066001225001049
4. *Denisov S.*, *Dolgikh V.*, *Khripchenko S.*, *Kolesnichenko I.*, *Nikulin L.* The effect of traveling and rotating magnetic fields on the structure of aluminum alloy during its crystallization in a cylindrical crucible. Magnetohydrodynamics. 2014. Vol. 50, no. 4. P. 407–422. DOI: 10.22364/mhd.50.4.8
5. *Al-Omari K.*, *Roósz A.*, *Rónaföldi A.*, *Veres Z.* Effect of Forced Melt Flow on Al–Si Eutectic-Alloy Microstructures. Crystals. 2022. Vol. 12, no. 5. 731. DOI: 10.3390/cryst12050731
6. *Timofeev V.*, *Pervukhin M.*, *Vinter E.*, *Sergeev N.* Behavior of non-conducting particles in molten aluminium cast into electromagnetic molds. Magnetohydrodynamics. 2020. Vol. 56, no. 4. P. 459–472. DOI: 10.22364/mhd.56.4.10
7. *Liu D.-d.*, *Zhou Y.-j.*, *Yang R.*, *et al.* Effect of electromagnetic stirring current on the mechanical properties of Cu-15Ni-8Sn alloy and its mechanism of inducing dendrite refinement and Sn distribution homogenization. Materials Today Communications. 2023. Vol. 37. 107224. DOI: 10.1016/j.mtcomm.2023.107224
8. *Grants I.*, *Gerbeth G.* The suppression of temperature fluctuations by a rotating magnetic field in a high aspect ratio Czochralski configuration. Journal of Crystal Growth. 2007. Vol. 308, no. 2. P. 290–296. DOI: 10.1016/j.jcrysgro.2007.09.002
9. *Liu H.*, *Zeng Z.*, *Qiu Z.*, *Yin L.*, *Xiao Y.* Effect of rotating magnetic field on instabilities of thermocapillary flow in a Czochralski silicon melt pool. Physics of Fluids. 2020. Vol. 32, no. 10. DOI: 10.1063/5.0024416

10. *Davidson P.A.*, *Hunt J.C.R.* Swirling recirculating flow an a liquid-metal column generated by a rotating magnetic field. Journal of Fluid Mechanics. 1987. Vol. 185. P. 67–106. DOI: 10.1017/s0022112087003082

11. *Kolesnichenko I.*, *Khalilov R.*, *Khripchenko S.*, *Pavlinov A.* MHD-stirrer for cylindrical molds of continuous casting machines fabricated aluminium alloy. Magnetohydrodynamics. 2012. Vol. 48, no. 1. P. 221–233.

12. *Kolesnichenko I.*, *Pavlinov A.*, *Khalilov R.* Movement of solid-liquid interface in gallium alloy under the action of rotating magnetic field. Magnetohydrodynamics. 2013. Vol. 49, no. 1/2. P. 191–199. DOI: 10.22364/mhd.49.1-2.23

13. *Räbiger D.*, *Eckert S.*, *Gerbeth G.*, *Franke S.*, *Czarske J.* Flow structures arising from melt stirring by means of modulated rotating magnetic fields. Magnetohydrodynamics. 2012. Vol. 48, no. 1. P. 213–220. DOI: 10.22364/mhd.48.1.24

14. *Losev G.L.*, *Kolesnichenko I.V.*, *Khalilov R.I.* Control of the metal crystallization process by the modulated traveling magnetic field. Journal of Physics: Conference Series. 2018. Vol. 1128. 012051. DOI: 10.1088/1742-6596/1128/1/012051

15. *Nikrityuk P.A.*, *Ungarish M.*, *Eckert K.*, *Grundmann R.* Spin-up of a liquid metal flow driven by a rotating magnetic field in a finite cylinder: A numerical and an analytical study. Physics of Fluids. 2005. Vol. 17, no. 6. DOI: 10.1063/1.1897323

16. *Vogt T.*, *Grants I.*, *Räbiger D.*, *Eckert S.*, *Gerbeth G.* On the formation of Taylor–Görtler vortices in RMF-driven spin-up flows. Experiments in Fluids. 2011. Vol. 52, no. 1. P. 1–10. DOI: 10.1007/s00348-011-1196-x

17. *Nikrityuk P.A.*, *Ungarish M.*, *Eckert K.*, *Grundmann R.* Losev, G. and Shvydkiy, E. and Sokolov, I. and Pavlinov, A. and Kolesnichenko, I.. Magnetohydrodynamics. 2019. Vol. 55, no. 1/2. P. 107–114. DOI: 10.22364/mhd.55.1-2.13

18. *Khripchenko S.Y.*, *Dolgikh V.M.*, *Siraev R.R.* Distribution of titanium diboride microparticles introduced into aluminum ingot by MHD-stirring of a crystallizing melt. Computational Continuum Mechanics. 2022. Vol. 15, no. 4. P. 438–448. DOI: 10.7242/1999-6691/2022.15.4.34

19. *Kolesnichenko I.*, *Okatev R.* Equalisation the toroidal and poloidal kinetic energies of liquid metal stirring flow. The European Physical Journal Plus. 2024. Vol. 139, no. 9. DOI: 10.1140/epjp/s13360-024-05629-7

20. *Kolesnichenko I.*, *Mamykin A.*, *Khalilov R.* Electromagnetic liquid metal stirrer: verification of the electromagnetic part of the problem. Bulletin of Perm University. Physics. 2022. No. 4. P. 45–51. DOI: 10.17072/1994-3598-2022-4-45-51

21. *Ozernykh V.S.*, *Losev G.L.*, *Golbraikh E.*, *Kolesnichenko I.V.* Initial stage of formation of vortex flow in an inductor with counter-rotating magnetic fields. Computational Continuum Mechanics. 2023. Vol. 16, no. 4. P. 493–503. DOI: 10.7242/1999-6691/2023.16.4.41

22. *Losev L.G.*, *Okatev R.S.* Measurement of the Dependence of the Effective Electrical Conductivity of Liquid Metals with Solid Particles on the Volume Fraction of an Impurity. Russian Metallurgy (Metally). 2024. Vol. 2024. P. 65–71. DOI: 10.1134/s0036029524701374

23. *Kolesnichenko I.V.*, *Khalilov R.I.* Extremum in the dependence of the head generated by electromagnetic pump of liquid metal on feeding current frequency. Computational Continuum Mechanics. 2022. Vol. 15, no. 4. P. 495–506. DOI: 10.7242/1999-6691/2022.15.4.38

24. *Nigmatulin R.I.* Dynamics of Multiphase Media. Vol. 1. New York: Hemisphere, 1991. 507 p.

25. *Ding J.*, *Gidaspow D.* A bubbling fluidization model using kinetic theory of granular flow. AIChE Journal. 1990. Vol. 36, no. 4. P. 523–538. DOI: 10.1002/aic.690360404

26. *Shirvanian P.A.*, *Calo J.M.*, *Hradil G.* Numerical simulation of fluid–particle hydrodynamics in a rectangular spouted vessel. International Journal of Multiphase Flow. 2006. Vol. 32, no. 6. P. 739–753. DOI: 10.1016/j.ijmultiphaseflow.2006.02.009

27. *Chapman S.*, *Cowling T.G.* The Mathematical Theory of Non-uniform Gases: An Account of the Kinetic Theory of Viscosity, Thermal Conduction and Diffusion in Gases. Cambridge University Press, 1990. 423 p.

28. *Gidaspow D.* Multiphase Flow and Fluidization: Continuum and Kinetic Theory Descriptions. Elsevier Science, 1994. 467 p.

29. *Goldhirsch I.* Introduction to granular temperature. Powder Technology. 2008. Vol. 182, no. 2. P. 130–136. DOI: 10.1016/j.powtec.2007.12.002

30. *Wang J.* Continuum theory for dense gas-solid flow: A state-of-the-art review. Chemical Engineering Science. 2020. Vol. 215. 115428. DOI: 10.1016/j.ces.2019.115428

31. *Lun C.K.K.*, *Savage S.B.*, *Jeffrey D.J.*, *Chepurniy N.* Kinetic theories for granular flow: inelastic particles in Couette flow and slightly inelastic particles in a general flowfield. Journal of Fluid Mechanics. 1984. Vol. 140. P. 223–256. DOI: 10.1017/s0022112084000586

32. *Saffman P.G.* The lift on a small sphere in a slow shear flow. Journal of Fluid Mechanics. 1965. Vol. 22, no. 2. P. 385–400. DOI: 10.1017/s0022112065000824

33. *Leenov D.*, *Kolin A.* Theory of Electromagnetophoresis. I. Magnetohydrodynamic Forces Experienced by Spherical and Symmetrically Oriented Cylindrical Particles. The Journal of Chemical Physics. 1954. Vol. 22, no. 4. P. 683–688. DOI: 10.1063/1.1740149

34. *Zhang L.*, *Wang S.*, *Dong A.*, *Gao J.*, *Damoah L.N.W.* Application of Electromagnetic (EM) Separation Technology to Metal Refining Processes: A Review. Metallurgical and Materials Transactions B. 2014. Vol. 45, no. 6. P. 2153–2185. DOI: 10.1007/s11663-014-0123-y

35. *Syamlal M.*, *O'Brien T.J.* Simulation of granular layer inversion in liquid fluidized beds. International Journal of Multiphase Flow. 1988. Vol. 14, no. 4. P. 473–481. DOI: 10.1016/0301-9322(88)90023-7

36. *Dallavalle J.M.* Micromeritics: The Technology of Fine Particles. Pitman, 1948. 555 p.

37. *Garside J.*, *Al-Dibouni M.R.* Velocity-Voidage Relationships for Fluidization and Sedimentation in Solid-Liquid Systems. Industrial & Engineering Chemistry Process Design and Development. 1977. Vol. 16, no. 2. P. 206–214. DOI: 10.1021/i260062a008

38. *Dobosz A.*, *Plevachuk Y.*, *Sklyarchuk V.*, *Sokoliuk B.*, *Gancarz T.* Thermophysical properties of the liquid Ga–Sn–Zn eutectic alloy. Fluid Phase Equilibria. 2018. Vol. 465. P. 1–9. DOI: 10.1016/j.fluid.2018.03.001

39. *Williams B.S.*, *Marteau D.*, *Gollub J.P.* Mixing of a passive scalar in magnetically forced two-dimensional turbulence. Physics of Fluids. 1997. Vol. 9, no. 7. P. 2061–2080. DOI: 10.1063/1.869326

Authors' Details:

Okatev Roman Sergeevich (corr.), Junior researcher; e-mail: okatev.r@icmm.ru; ORCID: 0000-0003-2741-1531

Losev Gennadiy Leonidovich, Researcher; e-mail: losev.g@icmm.ru; ORCID: 0000-0002-8028-3041

Kolesnichenko Ilya Vladimirovich, Head of the Laboratory; e-mail: kiv@icmm.ru; ORCID: 0000-0001-9378-5334